Label-free deep UV microscopy in oral cytology: a step towards stain-free diagnostics

SUMSUM P. SUNNY,[1,2,3,5] JIABIN CHEN,[1] YIHAN WANG,[1] BHARGHABI PAULMAJUMDER,[2] BOFAN SONG,[1] A. R. SUBHASHINI,[4] VIJAY PILLAI,[2] MONI A. KURIAKOSE,[3] PRAVEEN BIRUR N,[4] AMRITHA SURESH,[2,3] AND RONGGUANG LIANG[1,*] [iD]

[1] *James C. Wyant College of Optical Sciences, University of Arizona, Tucson AZ, USA*
[2] *Department of Head and Neck Oncology, Mazumdar Shaw Medical Center, Bangalore, India*
[3] *Integrated Head and Neck Oncology Program (DSRG-5), Mazumdar Shaw Medical Foundation, Bangalore, India*
[4] *Department of Oral Medicine and Radiology, KLE Society's Institute of Dental Sciences, Bangalore, India*
[5] *sumsumsp@gmail.com*
[*] *rliang@optics.arizona.edu*

Abstract: Oral cancer remains a significant global health challenge. Early detection is essential for improving prognostic outcomes, yet current diagnostic practices are hindered by the invasive nature of biopsies and the reliance on staining methods. This study presents a low-cost, label-free deep ultraviolet (UV) microscopy system, integrated with artificial intelligence (AI), for analyzing unstained cytology specimens. Leveraging the absorption properties of nuclei under UV light, this technology produces high-resolution molecular images, enabling real-time, automated, and objective analysis of cellular and nuclear morphology. Forty patients with oral lesions—spanning benign, oral potentially malignant disorders (OPMD), and oral squamous cell carcinoma (OSCC)—participated in this study. Cytology nuclei were segmented using a deep learning-based U-Net architecture, and key nuclear features, including intensity, solidity, eccentricity, and axis ratio, were extracted and analyzed. These features demonstrated high sensitivity (>80%) and specificity (>79%) in distinguishing diagnostic groups. Furthermore, unsupervised clustering based on these features effectively classified patient cohorts, underscoring its potential for early diagnosis. The proposed method eliminates the need for staining, reduces processing time, and minimizes environmental impact, making it particularly suited for primary healthcare settings. By integrating advanced imaging with AI, this scalable approach addresses critical gaps in early oral cancer detection, offering significant potential to improve patient outcomes. Validation in larger and more diverse cohorts is required to enhance its clinical utility.

1. Introduction

Oral cancer has emerged as an important global health problem, particularly prevalent in the Indian subcontinent. The stage at which oral cancer is diagnosed plays a pivotal role in determining its oncological prognosis. Notably, in populations with a high prevalence of oral cavity cancers, nearly eighty percent of cases are preceded by asymptomatic yet clinically evident lesions known as oral potentially malignant disorders (OPMD) [1]. Despite the clear clinical diagnostic criteria and the ease of access to oral examination, a significant majority, over 70%, of oral cancers are diagnosed at advanced stages [2–4]. Effective early detection of oral cancer requires an easy-to-use, minimally-invasive technology that can be deployed at the point-of-care (POC) in a primary healthcare setting. Such a technology must deliver diagnostic accuracy comparable to the current gold standard, histopathology. As opposed to the histopathological gold standard after an invasive biopsy, brush cytology is preferred for patient compliance, as well as rapid and simple screening workflows.

While several adjuncts are available for identifying potentially malignant oral lesions, none currently offer reliable diagnoses in primary-healthcare settings that are comparable to histopathology [5]. Cytology is well-established in cervical cancer diagnostics, and the oral cavity is similarly well-suited to this approach. We have demonstrated artificial intelligence-based conventional [6] and molecular marker-based cytology [7] improve the accuracy of oral cytology. However, performing cytology staining in primary healthcare settings presents significant challenges. The preparation and use of staining methods are time-consuming, costly, and generate toxic waste, highlighting the need for stain-free imaging solutions [8]. To address this, we have developed a label-free technique with a low-cost, deep ultraviolet (UV) microscope for imaging unstained slides in oral cytology analysis. We hypothesize that unstained cytology using UV imaging provide objective interrogation of the cell morphology and its nuclear content to diagnose OPMD, oral, and oropharyngeal squamous cell carcinomas (OSCC).

The deep UV microscope utilizes the strong absorption properties of nuclei at wavelengths below 300 nm to produce high-resolution, label-free images [9–20]. This technology also enables real-time mapping of nuclei and proteins in live cells using a quantitative approach based on the extinction coefficient [9]. Continuous UV imaging for over six hours has been demonstrated to occur without causing cell death or affecting the motility and mitotic processes of live mammalian cells [9]. Additionally, absorbance at 280 nm and 260 nm, along with tryptophan's native fluorescence, was quantified to create detailed maps of nucleic acid mass, protein mass, and quantum yield in unlabeled cells. Despite these advancements, the widespread adoption of deep UV (DUV) imaging in biological research was historically constrained by the high costs of specialized light sources, detectors, and optical systems. However, recent technological progress has significantly reduced these barriers. The introduction of compact and affordable DUV light sources, including deep-UV LEDs [17] and low-cost excimer lamps [18], along with adaptations of consumer-grade CMOS sensors for UV detection through removal of microlens arrays and color filters [21], have enabled the development of low-cost DUV microscopes [19,20]. These advances have expanded the application of DUV imaging to point-of-care hematological diagnostics [12,20], rapid bone marrow adequacy assessments [10], label-free histological evaluations in cancers [8,16], and live-cell molecular mapping [9]. Building upon these technological improvements, our study applies a low-cost, label-free DUV imaging system for oral cytology, addressing the need for accessible and stain-free diagnostics in primary healthcare settings.

This reported study evaluates unstained cytology specimens obtained through minimally invasive brush biopsy, leveraging UV imaging to eliminate the need for staining while enabling high-resolution imaging without additional sample processing. Additionally, artificial intelligence (AI) supports quantitative analysis of diagnostic features, reducing inter-observer variability and providing automated, objective diagnoses. By integrating a stain-free sampling method with AI-driven automation, this approach offers a scalable and cost-effective solution for early detection in primary healthcare settings.

2. Methodology

2.1. Deep ultraviolet microscope

The uncovered deep UV microscope device is shown in Fig. 1(A). It has a spatial resolution of 0.45 μm and a field of view of 0.45 × 0.34 mm. It features a 265 nm LED source (Thorlabs M265D4) mounted on a heatsink tube for illumination, emitting light at a 120° angle at half-max intensity. To improve illumination uniformity, a UV diffuser (Thorlabs DGUV10-120) is incorporated. Transmitted light passing through the sample is collected by a UV objective lens with a numerical aperture (NA) of 0.36.. A custom-designed double lens serves as the tube lens, providing a magnification of 80x. The UV sensor, depicted in Fig. 1(B), is a modified low-cost SONY IMX219 CMOS sensor with an 8 MP pixel resolution, following the method reported by Wilkes

et al. [21] Fig. 1(B1) illustrates the schematic of the original pixel structure, including the microlens array and color filter array (CFA), while Fig. 1(B2) shows the pixel structure without these components. Figure 1(B3) shows the CMOS sensor with its cover glass removed, while Fig. 1(B4) displays the sensor after both the microlens array and color filter array (CFA) have been removed, revealing the sensing region clearly at the center. The modified sensor is covered with a fused silica window, making it sensitive to deep UV light. This silicon photodiode, devoid of the lenslet array and CFA, is capable of detecting light wavelengths down to 200 nm.
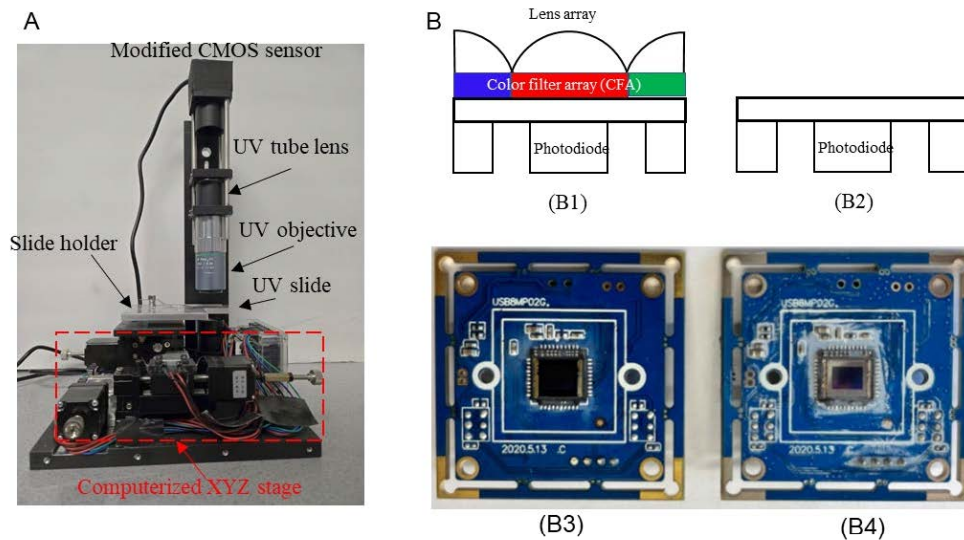

Fig. 1. Custom low-cost deep ultraviolet microscope. (A) The microscope without covers, (B1) schematic diagram of the pixel structure of a CMOS sensor with microlens array and color filter array (CFA), (B2) the pixel structure without microlens array and CFA, (B3) the picture of a CMOS sensor with the cover glass window removed, and (B4) the picture of the CMOS sensor with microlens array and CFA removed, the processed sensor is sensitive to deep UV light.

After collecting a sample from a suspicious region in the oral cavity, the specimen can be prepared for analysis using one of two methods. It can either be spread directly onto the fused silica UV microscope slide or processed using the cytospin preparation technique to ensure an even distribution of cells. Once the sample is prepared on the slide, it is fixed with 50% ethanol to preserve cellular morphology and prevent degradation. The prepared slide is then mounted onto a slide holder that is integrated into a custom computerized XYZ stage driven by three NEMA11 stepper motors. This stage allows precise and automated control of the slide's position in three dimensions, enabling systematic scanning of the sample area. The XYZ stage ensures accurate alignment and smooth movement, which is critical for acquiring high-resolution images and for the subsequent application of quantitative analysis techniques. This streamlined process enhances the efficiency and reliability of sample imaging, making it suitable for diagnostic and research purposes. Figure 2(A) presents representative UV image of oral cells, while Fig. 2(B) shows an array of UV images from a single slide, which can be seamlessly stitched together.

2.2. Clinical testing

2.2.1. Sample collection and processing:

Forty Participants recruited in this study were those visiting the Head and Neck Oncology Services at Mazumdar Shaw Medical Center (NHH/AEC-CL-2024-1160), Bangalore, and Department of
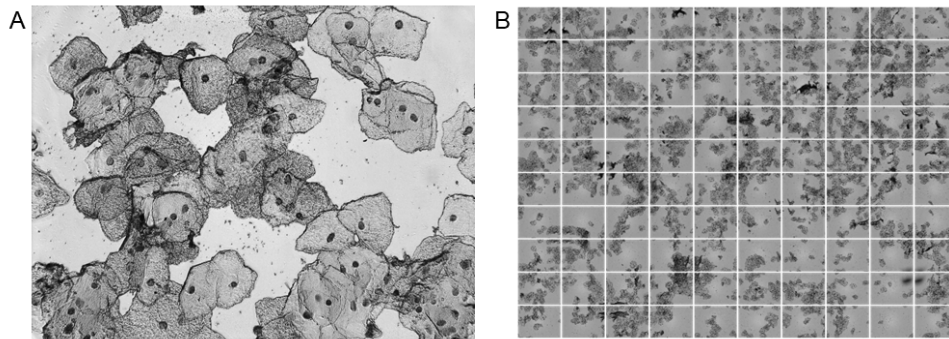
Fig. 2. Deep UV images of oral cells. (A) A typical UV image of oral cells (image dimension: 3.2 mm × 2.7 mm), and (B) an array of UV images obtained from one slide with the automatic scanning process (each sub-image dimension: 0.45 mm × 0.34 mm).

Oral Medicine and Radiology, KLE Society's Institute of Dental Science, Bangalore. Written informed consent was obtained from all eligible participants. Oral cell samples were collected by brush biopsy from individuals aged 18 and above who had been diagnosed with suspected benign, oral potentially malignant disorders (OPMDs) or cancer. Participants with acute illnesses or severe systemic diseases were excluded from the study. The brush biopsy samples were collected in BD Surepath (BD Biosciences, Cat No: 491253) and washed with PBS prior to processing. Slides were prepared using a Cytospin (Cytospin 4, Thermoscientific) and fixed in 50% ethanol before imaging. Imaging was conducted across slide and an average of 40 Regions of Interest (ROIs; range: 24-85) were selected manually for imaging based on the presence of oral epithelial cells.

2.2.2. Segmentation of nuclei

We developed a deep learning-based technique for the segmentation of nuclei in epithelial cells [22,23]. Training data were annotated by a clinical expert to create nuclei masks in UV images, using MATLAB 2019 Image Labeler. The segmentation model was based on a U-Net architecture [24], employing convolutional neural network (CNN) filters. The model follows the standard encoder–decoder architecture with skip connections but is modified in the following key ways: (1) we reduced the number of filters per layer (starting from 16 instead of 64 in the original U-Net), and (2) we used fewer total parameters, making it suitable for training on small datasets without overfitting. The encoder comprises five convolutional blocks, each consisting of two 3×3 Conv2D layers with ReLU activation, he-normal weight initialization, Batch Normalization, and Dropout (0.1), followed by 2×2 MaxPooling for spatial down sampling. The number of filters used in the encoder are 16, 16, 32, 64, and 128 respectively across the five blocks. In the decoder path, we use Conv2DTranspose layers for upsampling, with the following filter sizes: 64, 32, 16, and 16 (kernel size 2×2, stride 2, and same padding). Each upsampling step is followed by skip connections that concatenate the corresponding encoder feature maps. These are then passed through two Conv2D layers (with filter sizes mirroring the corresponding upsampling layer), BatchNormalization, and Dropout (0.1), matching the encoder structure. The final output layer uses a 1×1 Conv2D with two classes filters and a softmax activation to produce a pixel-wise segmentation map.

The Adam optimizer was used, with a one-cycle learning rate (LR) policy that gradually increases the learning rate from a lower bound to a maximum value and then decreases it, helping the model escape sharp minima and improve generalization. A callback function monitored the Intersection-over-Union (IoU) score, saving the best-performing model after each epoch if an

improvement in IoU was observed. Training was conducted with a batch size of eight. Model performance was evaluated using the IoU score with a threshold of 0.5, and the F1 score (with a threshold of 0.5) was also used as an additional metric to assess the segmentation quality. The total loss was a combination of focal loss and Dice loss, which aims at enhancing model performance. This approach ensures robust and accurate nucleus segmentation in UV microscopy images.

2.2.3. Feature extraction and classification

Segmentation performance declined in regions with clustered cells or closely positioned nuclei, often leading to segmentation errors. While morphological features were extracted from the predicted segmentation masks, accurate feature analysis in regions with closely packed or overlapping nuclei required further refinement. Although the U-Net-based model produces binary segmentation masks, these masks often contain coarse boundaries and merged regions due to the complexity of nuclear clustering. To enhance segmentation precision, additional postprocessing steps were applied [25]. First, Otsu's thresholding was used to sharpen the edges of binary masks and suppress faint or noisy foreground artifacts that may persist after initial segmentation. Next, small isolated noise components were removed to eliminate non-nuclear debris. Morphological operations were then applied to generate "sure foreground" and "sure background" regions, providing accurate initialization points for watershed segmentation, which is critical for separating adjacent or touching nuclei. Finally, region properties were extracted from the refined masks for subsequent intensity-based feature analysis. This postprocessing pipeline ensured robust and reliable segmentation, enabling accurate downstream morphological quantification. The watershed algorithm was then applied to accurately segment individual components within the image based on the prediction from the segmentation model. Additionally, the region props function from the skimage Python library was used to extract the intensity image corresponding to each region from the original image.

Various nuclear features were extracted (using python library), including nuclear intensity, perimeter, minor and major axis lengths, convex area, eccentricity, nuclear area, equivalent diameter, and solidity. To simplify the feature space, dimensionality reduction techniques were applied, followed by unsupervised classification to group nuclei based on shared characteristics. For each patient, a statistical aggregate was created using the extracted features from all their nuclei, forming a comprehensive feature vector. Metrics such as mean, maximum, and standard deviation of the nuclear features were calculated for each patient, and exploratory data analysis was conducted to identify significant features that differentiate among various cohorts. This approach enables robust statistical characterization and potential biomarker discovery across patient groups.

3. Results

3.1. Patient distribution

The brush biopsy was performed in 40 oral lesions who are clinically diagnosed with oral cancer (n = 16), OPMDs (n = 18), and benign (n = 8). Out of 18 OPMDs, eight patients underwent incisional biopsy, seven were diagnosed as dysplastic lesions and one as lichen planus. All oral cancer cases were diagnosed as Oral Squamous Cell Carcinoma (OSCC). The median age of the cohort was 50 years (range: 18-72). Among the patients, 82.5% had the habit of tobacco usage with the gender ratio being 3.4 (M/F). The majority (58%) of the lesions were from buccal mucosa.

3.2. Nucleus segmentation and classification

Segmentation of nuclei: The total number of UV images (n = 1,459) were acquired, including benign (n = 191), OPMD (n = 640), and cancer (n = 628) cases. The nuclei were manually segmented by the trained researcher and then checked by an expert. Any mistakes were corrected before using the data for training to make sure the segmentations were accurate. Of these, 909 images were manually annotated for nuclear segmentation and used to train the segmentation model. The UV cytology images (n = 909) and masks were augmented (n = 4545) four times by horizontal flip, vertical flip, image enhancement (factors: 0.7 and 1.2). The image enhancement was performed to improve the brightness of the image using the python library pillow and 0.7 and 1.2 are brightness parameters from the current brightness. The mean IoU for segmentation in training and validation was 0.85 and 0.80 (n = 90) respectively (*S* Fig. 1).

The number of nuclei segmented included benign (n = 811), OPMD (n = 2,880), and cancer cases (n = 3,255). We analyzed the cell-wise distribution of features. The OPMD nuclear intensity showed bimodal distribution with high variance (**S** Fig. 2) compared to the cancer and benign lesions. The nuclei of atypical cells from cancer and OPMD patients showed a higher density (lower intensity) compared to cells from benign (Fig. 3(A)).
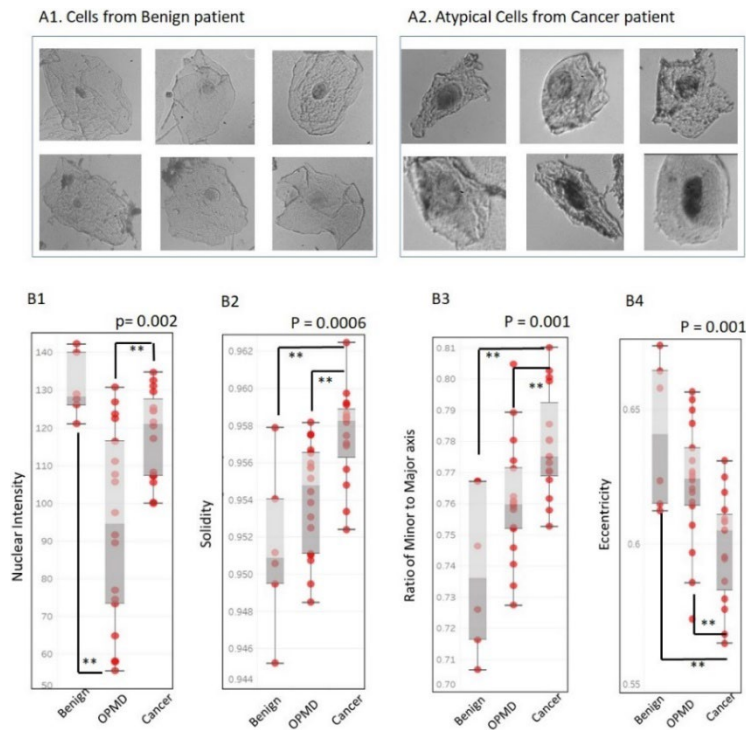

Fig. 3. Prominent nuclear features using UV imaging. UV cytology image of cells (cropped) from benign (A1) and atypical cells from cancer patients (A2), with a field of view approximately 70 μm. Nuclear features extracted from cells (mean value of each patient) were depicted B1-B4. Features significantly separated benign, OPMD and cancer patients. ** p < 0.005

Distribution of features: The nuclear features were averaged on a per-patient basis. Nuclear intensity, the ratio of minor to major axis, eccentricity, and solidity were able to distinguish between benign, OPMD, and cancer (Fig. 3(B)) significantly (p < 0.005). Solidity and the axis ratio exhibited an increasing trend, while eccentricity showed a decreasing trend from benign

to cancer (Figure 3(B2-B4)). The average intensity of the nuclei in the OPMD patients was lower compared to that of benign cells. In the ROC analysis, solidity, axis ratio, and eccentricity differentiated cancer cohorts from OPMD and benign groups with a sensitivity above 80% and a specificity of 79%. Nuclear intensity distinguished OPMD from benign samples with a sensitivity of 77.78% and a specificity of 83.33% (Table 1)

Table 1. Classification using Nuclear features

Classification	Parameters	Nuclear Intensity	Solidity	Axis Ratio	Eccentricity
Cancer Vs OPMD + Benign	Sensitivity	68.75	81.25	81.25	81.25
	Specificity	54.17	62.50	79.17	79.17
	Area Under the Curve (AUC)	0.654	0.846	0.815	0.823
OPMD Vs Benign	Sensitivity	77.78	88.89	77.78	100.00
	Specificity	83.33	50.00	66.67	50.00
	Area Under the Curve (AUC)	0.87	0.694	0.722	0.657

Unsupervised classification cohort using nuclear features: The dataset consisted of 40 patients with 36 features, including the mean, minimum, maximum, and standard deviation of nine nuclear features. The data were scaled using a standard scaler. The correlation between the features was analyzed using PCA. Ten principal components (PCs), which explained 92% variation in data were selected for the unsupervised learning **(Figure S3)**. Hopkin score calculated for PC showed a value of 0.64, indicating that the dataset tended to cluster. The distribution PCs (PC1 and PC2) showed clustering according to the clinical diagnosis (Fig. 4(A)). The benign patients formed a clearly distinct cluster compared to OPMD and cancer. Hierarchical clustering using the Ward method revealed three distinct clusters (Fig. 4(B), Dendrogram) [26]. The distribution of data according to hierarchical clustering and diagnosis (Fig. 4(C)) showed patients with cancer primarily grouped in cluster 0 (n = 10/16), while cluster 1 was formed by OPMD (14/18).
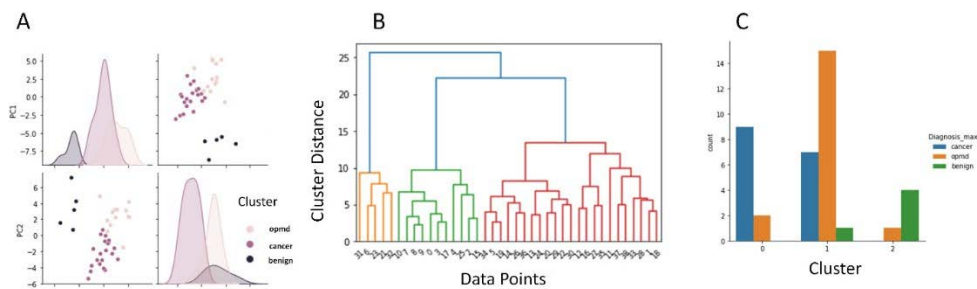

Fig. 4. Unsupervised learning of nuclear feature: Distribution PCs (PC1 and PC2) showed clustering according to the clinical diagnosis (A). Dendogram (B) showed formation of three clusters according to nuclear features. Cancer and OPMD shared similar features(C).

4. Discussion

One of the significant advantages of our approach is the elimination of the need for staining, which addresses the practical challenges associated with staining in primary healthcare settings. The use of UV imaging provides high-resolution images, enabling detailed morphological analysis of cells and nuclei. This is crucial for identifying abnormal cells based on features such as nuclear size, shape, and the nucleus-to-cytoplasm (N/C) ratio, which are critical indicators of

malignancy. Deep-UV microscopy has been proven as a robust technique for detecting and grading neutropenia. The automated framework accurately segments and classifies live, unstained blood cells in a smear, distinguishing patients with moderate and severe neutropenia from healthy samples within minutes [27].

Our study involved a diverse cohort with a significant proportion of participants using tobacco, a known risk factor for oral cancer. The patient-wise analysis of nuclear features such as solidity, the ratio of minor to major axis, and eccentricity demonstrated significant differences between benign, OPMD, and cancer cohorts, with high sensitivity and specificity. The results underscore the clinical relevance of these features in the early detection of oral cancer. This highlights the robustness of the AI model and its potential for deployment in real-time diagnostic workflows. The proposed method eliminates the requirements for dyes, resulting in time and cost savings. This approach allows for immediate testing after specimen collection.

Despite promising results, there are a few limitations to our study. The relatively small sample size and the bimodal distribution of nuclear intensity in OPMD cases suggest the need for larger, more diverse cohorts to validate our findings. Furthermore, while our UV imaging system is cost-effective and eliminates the need for dyes, the implementation in resource-limited settings requires further evaluation to ensure feasibility and accessibility. Future research should focus on refining the AI algorithms to enhance accuracy and exploring the integration of cellular features. Additionally, longitudinal studies are necessary to assess the prognostic value of the identified nuclear features and their correlation with clinical outcomes.

Additionally, while the segmentation performance achieved with our modified U-Net model was satisfactory for this pilot study, we recognize its limitations, particularly in challenging cases with clustered nuclei. Future work will explore the integration of pretrained models and more advanced segmentation architectures, including vision transformer-based networks, which have shown promise in biomedical image segmentation tasks. These approaches, combined with expanded datasets and advanced data augmentation strategies, have the potential to further improve segmentation accuracy and enhance the robustness of feature extraction in oral cytology applications.

In conclusion, our study provides a compelling case for the use of a low-cost, label-free UV imaging system combined with AI for the early detection and classification of OPMD and OSCC. This approach addresses critical gaps in current diagnostic practices, offering a practical and scalable solution for primary healthcare settings. By leveraging advanced imaging and AI technologies, we can significantly enhance the early diagnosis and management of oral cancer, ultimately improving patient outcomes.

References

1. M. Idrees, C. S. Farah, and P. Sloan, "Oral brush biopsy using liquid-based cytology is a reliable tool for oral cancer screening: A cost-utility analysis," Cancer Cytopathol. **130**(9), 740–748 (2022).
2. O. Felthaus, T. Ettl, M. Gosau, *et al.*, "Cancer stem cell-like cells from a single cell of oral squamous carcinoma cell lines," Biochem. Biophys. Res. Commun. **407**(1), 28–33 (2011).
3. S. S. Patel, K. A. Shah, M. J. Shah, *et al.*, "Cancer stem cells and stemness markers in oral squamous cell carcinomas," Asian Pac. J. Cancer Prev. **15**(20), 8549–8556 (2014).
4. C. Laprise, H. P. Shahul, S. A. Madathil, *et al.*, "Periodontal diseases and risk of oral cancer in Southern India: Results from the HeNCe Life study," Int J Cancer. **139**(7), 1512–1519 (2016).
5. P. Mendonca, S. P. Sunny, U. Mohan, *et al.*, "Non-invasive imaging of oral potentially malignant and malignant lesions: A systematic review and meta-analysis," Oral Oncol. **130**, 105877 (2022).

6. S. Sunny, A. Baby, B. L. James, *et al.*, "A smart tele-cytology point-of-care platform for oral cancer screening," PLoS One **14**(11), e0224885 (2019).

7. D. R. R. Sunny SP, A. Hariharan, *et al.*, "CD44-SNA1 integrated cytopathology for delineation of high grade dysplastic and neoplastic oral lesions," PLoS One **18**(9), e0291972 (2023).

8. Y. Zhang, B. Huang, W. Dai, *et al.*, "Label-free and non-destructive histology of unprocessed biological tissues with ultraviolet single-plane illumination microscopy," APL Photonics **9**(1), 016116 (2024).

9. B. J. Zeskind, C. D. Jordan, W. Timp, *et al.*, "Nucleic acid and protein mass mapping by live-cell deep-ultraviolet microscopy," Nat. Methods **4**(7), 567–569 (2007).

10. F. Jamme, S. Kascakova, S. Villette, *et al.*, "Deep UV autofluorescence microscopy for cell biology and tissue histology," Biol. Cell **105**(7), 277–288 (2013).

11. S. Soltani, A. Ojaghi, and F. E. Robles, "Deep UV dispersion and absorption spectroscopy of biomolecules," Biomed. Opt. Express **10**(2), 487–499 (2019).

12. A. Ojaghi, G. Carrazana, C. Caruso, *et al.*, "Label-free hematology analysis using deep-ultraviolet microscopy," Proc. Natl. Acad. Sci. U.S.A. **117**(26), 14779–14789 (2020).

13. F. Strohl, D. L. Wolfson, I. S. Opstad, *et al.*, "Label-free superior contrast with c-band ultra-violet extinction microscopy," Light: Sci. Appl. **12**(1), 56 (2023).

14. M. C. Cheung, J. G. Evans, B. McKenna, *et al.*, "Deep ultraviolet mapping of intracellular protein and nucleic acid in femtograms per pixel," Cytometry, Part A **79A**(11), 920–932 (2011).

15. N. Kaza, A. Ojaghi, and F. E. Robles, "Hemoglobin quantification in red blood cells via dry mass mapping based on UV absorption," J. Biomed. Opt. **26**(08), 086501 (2021).

16. S. Soltani, A. Ojaghi, H. Qiao, *et al.*, "Prostate cancer histopathology using label-free multispectral deep-UV microscopy quantifies phenotypes of tumor aggressiveness and enables multiple diagnostic virtual stains," Sci. Rep. **12**(1), 9329 (2022).

17. V. Gorti, N. Kaza, E. K. Williams, *et al.*, "Compact and low-cost deep-ultraviolet microscope system for label-free molecular imaging and point-of-care hematological analysis," Biomed. Opt. Express **14**(3), 1245–1255 (2023).

18. D. Dhankhar and P. M. Rentzepis, "Techniques for Constructing Ultra Low Cost Deep Ultraviolet Transmission Microscopes," IEEE Access **11**, 41964–41969 (2023).

19. V. Gorti, K. McCubbins, D. Houston, *et al.*, "Quantifying UV-induced photodamage for longitudinal live-cell imaging applications of deep-UV microscopy," Biomed. Opt. Express **16**(1), 208–221 (2025).

20. V. Gorti, A. R. Subramanian, A. Ojaghi, *et al.*, "Rapid, point-of-care bone marrow aspirate adequacy assessment via deep ultraviolet microscopy," Lab. Invest. **105**(5), 104102 (2025).

21. T. C. Wilkes, A. J. McGonigle, T. D. Pering, *et al.*, "Ultraviolet imaging with low cost smartphone sensors: development and application of a Raspberry Pi-based UV camera," Sensors **16**(10), 1649 (2016).

22. J. Lee, H. Kim, H. Cho, *et al.*, "Deep-learning-based label-free segmentation of cell nuclei in time-lapse refractive index tomograms," IEEE Access **7**, 83449–83460 (2019).

23. M. S. Alom, A. Daneshkhah, N. Acosta, *et al.*, "Deep learning-driven automatic nuclei segmentation of live-cell chromatin-sensitive partial wave spectroscopic microscopy imaging," Opt. Express **32**(25), 45052–45074 (2024).

24. O. Ronneberger, P. Fischer, and T. Brox, "U-net: Convolutional networks for biomedical image segmentation," In *Medical image computing and computer-assisted intervention–MICCAI 2015: 18th international conference, Munich, Germany, October 5-9, 2015, proceedings, part III 18* (pp. 234–241). Springer international publishing, (2015).

25. P. S. Sumsum and A. K. Sunny, "Oral epithelial cell segmentation from fluorescent multichannel cytology images using deep learning," Comput. Methods Programs in Biomed. **227**(3), 107205 (2022).

26. F. Murtagh and P. Legendre, "Ward's hierarchical agglomerative clustering method: which algorithms implement Ward's criterion?" J. Classificat. **31**(3), 274–295 (2014).

27. A. Ojaghi, P. Casteleiro Costa, C. Caruso, *et al.*, "Label-free automated neutropenia detection and grading using deep-ultraviolet microscopy," Biomed. Opt. Express **12**(10), 6115–6128 (2021).